2008

Use of Variable Incidence Angle for Glide Slope Control of Autonomous Parafoils

Nathan Slegers
George Fox University, nslegers@georgefox.edu

Eric Beyer
Georgia Institute of Technology - Main Campus

Mark Costello
Georgia Institute of Technology - Main Campus

Use of Variable Incidence Angle for Glide Slope Control of Autonomous Parafoils

Nathan Slegers*
University of Alabama in Huntsville, Huntsville, Alabama 35899
and
Eric Beyer† and Mark Costello‡
Georgia Institute of Technology, Atlanta, Georgia 30332

Strictly speaking, most autonomous parafoil and payload systems possess only lateral control, achieved by right and left parafoil brake deflection. An innovative technique to achieve direct longitudinal control through incidence angle changes is reported. Addition of this extra control channel requires simple rigging changes and an additional servoactuator. The ability of incidence angle to alter the glide slope of a parafoil and payload aircraft is demonstrated through a flight-test program with a microparafoil system. Results from the flight-test program are synthesized and integrated into a six degree-of-freedom simulation. The simulation model is subsequently used to assess the utility of glide slope control to improve autonomous flight control system performance. Through Monte Carlo simulation, impact point statistics with and without glide slope control indicate that dramatic improvements in impact point statistics are possible using direct glide slope control.

Nomenclature

$\mathbf{A}$, $\mathbf{B}$, $\mathbf{C}$	=	discrete linear model state-space matrices
A, B, C, P, Q, R, H	=	Lamb's coefficients for apparent mass, inertia, and spanwise camber
b	=	canopy span
C_{DS}	=	payload drag coefficient
$\bar{c}$	=	canopy main chord
$\bar{d}$	=	brake characteristic length
$\boldsymbol{F}_W$	=	weight vector in a body reference frame
$\boldsymbol{F}_S$	=	payload drag vector in a body reference frame
$\boldsymbol{F}_A$, $\boldsymbol{M}_A$	=	aerodynamic force and moment vectors in a body reference frame
$\boldsymbol{F}_{\mathrm{AM}}$, $\boldsymbol{M}_{\mathrm{AM}}$	=	apparent mass force and moment vectors in a body reference frame
H_p	=	discrete model predictive controller prediction horizon
I_T	=	inertia matrix of total system
I_{AM}, I_{AI}, I_H	=	apparent mass, inertia, and spanwise camber matrices
K_p, K_i	=	glide slope controller proportional and integral gains
K_{CA}, K_{CAB}	=	model predictive control state propagation matrices
K	=	model predictive control gain matrix
m	=	mass of the combined system including payload and canopy
p, q, r	=	angular velocity components in a body reference frame
$\tilde{p}$, $\tilde{q}$, $\tilde{r}$	=	angular velocity of the system in the canopy frame
r_{LOS}	=	line-of-site vector from parafoil to target
S^B_ω, S^C_ω	=	cross-product matrix of the angular velocity expressed in a body and canopy reference frame
$S^B_{\mathrm{CG},P}$	=	cross-product matrix of the vector from the mass center to aerodynamic center
$S^B_{\mathrm{CG},M}$	=	cross-product matrix of the vector from the mass center to apparent mass center
$S^B_{\mathrm{CG},C}$	=	cross-product matrix of the vector from the mass center to canopy rotation point
$S^C_{V_A}$	=	cross-product matrix of the parafoil aerodynamic velcoity
S_P, S_S	=	reference area of the parafoil canopy and payload
T_{AC}	=	transformation from aerodynamic to canopy frames
T_{BC}	=	transformation from body to canopy frames
u, v, w	=	velocity components of mass center in the body reference frame
$\tilde{u}$, $\tilde{v}$, $\tilde{w}$	=	velocity components of the aerodynamic center in the canopy reference frame
u_{SA}, v_{SA}, w_{SA}	=	aerodynamic velocities of the payload in the body frame
$\boldsymbol{V}_{A/I}$	=	velocity vector of the wind in an inertial reference frame
V_A, V_S	=	total aerodynamic speed of the parafoil canopy and payload
x, y, z	=	inertial positions of the system mass center
Γ	=	canopy incidence angle
ΔT	=	glide slope control sampling interval
Δx_c, Δy_c, Δz_c	=	distance vector components from mass center to the canopy rotation point in a body reference frame
Δx_p, Δy_p, Δz_p	=	distance vector components from the canopy rotation point to the aerodynamic center in a canopy reference frame
θ_{LOS}	=	angle of the line-of-sight vector

Presented as Paper 2526 at the Aerodynamic Decelerator Conference, Williamsburg, VA, 21–24 May 2007; received 11 May 2007; revision received 14 August 2007; accepted for publication 16 August 2007.

*Assistant Professor, Department of Mechanical and Aerospace Engineering. Member AIAA.
†Graduate Research Assistant, School of Aerospace Engineering. Member AIAA.
‡Sikorsky Associate Professor, School of Aerospace Engineering. Associate Fellow AIAA.

$\phi, \theta,$ = Euler roll, pitch, and yaw angles
ω_{LOS} = angular velocity of the line-of-sight vector

I. Introduction

PARAFOIL and payload systems are unique flight vehicles well suited to perform autonomous airdrop missions. These air vehicles are compact before parafoil deployment, lightweight, fly at low speed, and impact the ground with low velocity. The predominant control mechanism for parafoils is left and right brake deflection. When a right brake control input is executed, the right back corner of the parafoil canopy is pulled down by changing the length of the appropriate suspension lines. Canopy changes created by brake deflection subsequently cause predictable changes in aerodynamic loads which is leveraged for control of the vehicle. For most parafoils, deployment of the right brake causes a significant drag rise and a small lift increase on the right side of the parafoil canopy combined with slight right tilt of the canopy. The overall effect causes the parafoil to skid turn to the right when a right parafoil brake is activated [1]. Longitudinal control is more difficult to achieve. Ware and Hassell showed symmetric deflection of brakes to an angle of 45 deg as pitch control did not effectively change the trim angle of attack; it did cause an increase in the lift and drag values at trim conditions, but the lift–drag ratio remained effectively unchanged [2]. Symmetric brake deflection to an angle of 90 deg caused large changes in trim angle of attack with the canopy stalling, reducing the lift–drag ratio to a value of about 0.5. Human skydivers use weight shift for both longitudinal and lateral control. By shifting weight fore and aft, glide slope can be actively controlled and it permits accurate trajectory tracking, to include very accurate ground impact point control in the presence of relatively high atmospheric winds.

The bulk of current autonomous parafoil and payload aircraft employ right and left brake deflection for control, which, strictly speaking, permits only lateral control. These aircraft typically do not have a direct means of longitudinal control. Hence, autonomous controllers for these air vehicles are greatly challenged to track three-dimensional trajectories and impact a specific ground target point. The usual means to create some semblance of altitude control is through a weaving maneuver back and forth across a desired trajectory path to "dump" altitude as progress is made along the desired path [3–10]. Near the intended ground impact location, current autonomous systems either spiral over the target or S-turn to the target. A key to the success for these algorithms is accurate descent rate estimation which is difficult to accomplish and prone to error.

The work reported here creates a glide slope control mechanism intended for use on autonomous parafoil and payload aircraft. Rather than using weight shift or symmetric brake deflection, glide slope control is physically achieved by changing the longitudinal rigging of the parafoil and payload combination dynamically in flight. The extra degree of freedom of control requires simple rigging changes and the addition of one additional servoactuator to the system. A detailed description of the basic mechanical design of the glide slope control mechanism is provided next. Traditional parafoil dynamic models treat the canopy orientation fixed with respect to the payload [11–14]. These traditional models allow effects such as apparent mass to be easily incorporated. A new six degree-of-freedom model is created that includes changing canopy orientation with respect to the payload and model apparent mass effects in a complete manner.

When combined with traditional right and left brake control, glide slope control is an attractive feature for autonomous parafoil and payload aircraft because it allows the flight control laws to directly correct descent rate, thus eliminating the need for descent rate estimation and the resulting error induced into the final delivery error. The ability of this system to change glide slope in flight is demonstrated with flight-test results for an exemplar microparafoil and payload system. The microparafoil and payload system is fitted with a data logger equipped with a sensor suite that contains a global positioning system (GPS), accelerometers, gyroscopes, barometric altimeter, magnetometers, and servoposition, so that the complete state of the payload along with all control inputs can be recorded. These flight-test results are subsequently synthesized and incorporated into a six degree-of-freedom (DOF) parafoil simulation, and autonomous performance with and without glide slope control is reported. Monte Carlo simulations are performed to predict impact point statistics using only lateral control, and lateral/longitudinal control. Results indicate that a dramatic improvement in impact point statistics is realized with the addition of glide slope control.

II. Parafoil Dynamic Model

Figure 1 shows a schematic of a parafoil and payload system. With the exception of movable parafoil brakes, the parafoil canopy is considered to be a fixed shape once it has completely inflated. The combined system of the parafoil canopy and the payload are modeled with six DOF, including three inertial position components of the total system mass center as well as the three Euler orientation angles. A body frame is fixed at the system mass center with I_B forward and aligned with the top of the payload. Orientation of the parafoil canopy with respect to the payload is defined as the incidence angle Γ and is considered a control variable. Rotation of the canopy about point C allows tilting of the canopy lift and drag vectors resulting in changes in the equilibrium glide slope. The canopy rotation point C is in line with the rear suspension lines so that by shorting the front lines and lengthening the brake lines, a pure canopy rotation can be achieved. The aerodynamic center is defined as P.

The kinematic equations for the parafoil and payload system are provided in Eqs. (1) and (2). The common shorthand notation for trigonometric functions is employed where $\sin(\alpha) \equiv s_\alpha$, $\cos(\alpha) \equiv s_\alpha$, and $\tan(\alpha) \equiv t_\alpha$.

$$\begin{Bmatrix} \dot{x} \\ \dot{y} \\ \dot{z} \end{Bmatrix} = [T_{\text{IB}}]^T \begin{Bmatrix} u \\ v \\ w \end{Bmatrix} \tag{1}$$

$$\begin{Bmatrix} \dot{\phi} \\ \dot{\theta} \\ \dot{\psi} \end{Bmatrix} = \begin{bmatrix} 1 & s_\phi t_\theta & c_\phi t_\theta \\ 0 & c_\phi & -s_\phi \\ 0 & s_\phi / c_\theta & c_\phi / c_\theta \end{bmatrix} \begin{Bmatrix} p \\ q \\ r \end{Bmatrix} \tag{2}$$

The matrix T_{IB} represents the transformation matrix from an inertial reference frame to the body reference frame.

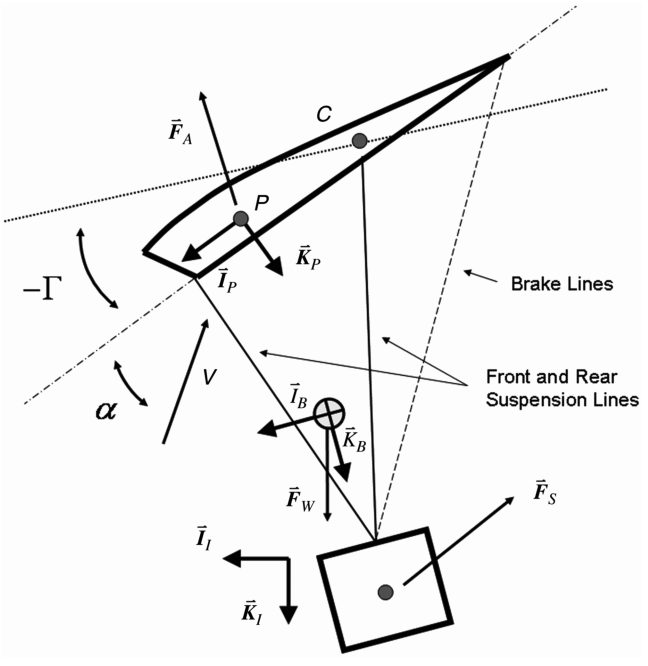

Fig. 1 Parafoil and payload schematic.

$$T_{\mathrm{IB}} = \begin{bmatrix} c_\theta c & c_\theta s & -s_\theta \\ s_\phi s_\theta c_\psi - c_\phi s & s_\phi s_\theta s_\psi + c_\phi c & s_\phi c_\theta \\ c_\phi s_\theta c_\psi + s_\phi s & c_\phi s_\theta s_\psi - s_\phi c & c_\phi c_\theta \end{bmatrix} \tag{3}$$

The dynamic equations are formed by summing forces and moments about the system mass center both in the body reference frame and equating to the time derivative of linear and angular momentum, respectively.

$$\begin{Bmatrix} \dot{u} \\ \dot{v} \\ \dot{w} \end{Bmatrix} = \frac{1}{m}(\boldsymbol{F}_W + \boldsymbol{F}_A + \boldsymbol{F}_S + \boldsymbol{F}_{\mathrm{AM}}) - S^B_\omega \begin{Bmatrix} u \\ v \\ w \end{Bmatrix} \tag{4}$$

$$\begin{Bmatrix} \dot{p} \\ \dot{q} \\ \dot{r} \end{Bmatrix} = [I_T]^{-1} \Bigg(\boldsymbol{M}_A + \boldsymbol{M}_{\mathrm{AM}} + S^B_{\mathrm{CG},P}\boldsymbol{F}_A + S^B_{\mathrm{CG},S}\boldsymbol{F}_S + S^B_{\mathrm{CG},M}\boldsymbol{F}_{\mathrm{AM}} - S^B_\omega [I_T] \begin{Bmatrix} p \\ q \\ r \end{Bmatrix} \Bigg) \tag{5}$$

The convention is used where the vector cross product of two vectors $\boldsymbol{r} = \{\, r_x \quad r_y \quad r_z \,\}^T$ and $\boldsymbol{F} = \{\, F_x \quad F_y \quad F_z \,\}^T$ both expressed in the A reference frame can be written as

$$S^A_r \boldsymbol{F} = \begin{bmatrix} 0 & -r_z & r_y \\ r_z & 0 & -r_x \\ -r_y & r_x & 0 \end{bmatrix} \begin{Bmatrix} F_x \\ F_y \\ Fz \end{Bmatrix} \tag{6}$$

Forces appearing in Eq. (4) have contributions from weight, aerodynamic loads on the canopy and payload, and apparent mass. Weights contribution is given in Eq. (7).

$$\boldsymbol{F}_W = mg \begin{Bmatrix} -s_\theta \\ s_\phi c_\theta \\ c_\phi c_\theta \end{Bmatrix} \tag{7}$$

Aerodynamic forces on the canopy appearing in Eq. (4) are expressed in the body reference frame; however, they are a function of the aerodynamics velocities in the canopy frame. Defining T_{BC} as the single axis transformation from the body to canopy reference frame by the incidence angle Γ, the aerodynamic velocity of the parafoil in the canopy frame is given in Eq. (8).

$$\begin{Bmatrix} \tilde{u} \\ \tilde{v} \\ \tilde{w} \end{Bmatrix} = [T_{\mathrm{BC}}] \Bigg[\begin{Bmatrix} u \\ v \\ w \end{Bmatrix} + S^B_\omega \Bigg(\begin{Bmatrix} \Delta x_c \\ \Delta y_c \\ \Delta z_c \end{Bmatrix} + [T_{\mathrm{BC}}]^T \begin{Bmatrix} \Delta x_p \\ \Delta y_p \\ \Delta z_p \end{Bmatrix} \Bigg) - [T_{\mathrm{IB}}]\boldsymbol{V}_{A/I} \Bigg] \tag{8}$$

The aerodynamic angles then become $\alpha = a\tan(\tilde{w}/\tilde{u})$ and $\beta = a\sin(\tilde{v}/V_A)$. Equation (9) defines the canopy aerodynamic forces in the body reference frame using T_{AC} as the transformation from aerodynamic to canopy frames by the angle α. Payload drag is defined in a similar manner in Eq. (10), in which u_{SA}, v_{SA}, and w_{SA} are payload aerodynamic velocities in the body frame.

$$\boldsymbol{F}_A = \frac{1}{2}\rho V_A^2 S_P [T_{\mathrm{BC}}]^T [T_{\mathrm{AC}}] \begin{Bmatrix} C_{D0} + C_{D\alpha 2}\alpha^2 \\ C_{Y\beta}\beta \\ C_{L0} + C_{L\alpha}\alpha + C_{L\alpha 3}\alpha^3 \end{Bmatrix} \tag{9}$$

$$\boldsymbol{F}_S = -\frac{1}{2}\rho V_S S_S C_{\mathrm{DS}} \begin{Bmatrix} u_{\mathrm{SA}} \\ v_{\mathrm{SA}} \\ w_{\mathrm{SA}} \end{Bmatrix} \tag{10}$$

Moments appearing in Eq. (5) have contributions from aerodynamic moments and apparent inertia, and from forces on the canopy and payload. Aerodynamic moments expressed in the body frame are given in Eq. (11).

$$\boldsymbol{M}_A = \frac{1}{2}\rho V_A^2 S_P [T_{\mathrm{BC}}]^T \begin{Bmatrix} b[C_{l\beta}\beta + (b/2V_A)C_{lp}\tilde{p} + (b/2V_A)C_{lr}\tilde{r}] + C_{l\delta a}(\delta_a + \bar{d}) \\ \bar{c}[C_{m0} + (\bar{c}/2V_A)C_{mq}\tilde{q}] \\ b[C_{n\beta}\beta + (b/2V_A)C_{np}\tilde{p} + (b/2V_A)C_{nr}\tilde{r}] + C_{n\delta a}(\delta_a + \bar{d}) \end{Bmatrix} \tag{11}$$

A body moving in a fluid places the fluid in motion. The result from accelerating the fluid is a rate of change in both its linear and angular momentum. Typical aircraft having large mass-to-volume ratios have negligible effects from the mass of the accelerating fluid. Parafoils with small mass-to-volume ratios can experience large forces and moments from accelerating fluid called "apparent mass" and "apparent inertia" because they appear as additional mass and inertia values in the final equations of motion, provided that their effects are not already covered by the aerodynamic coefficients. Kinetic energy of the fluid can be written as

$$2T = A\tilde{u}^2 + B\tilde{v}^2 + C\tilde{w}^2 + P\tilde{p}^2 + Q\tilde{q}^2 + R\tilde{r}^2 + 2H(\tilde{u}\,\tilde{q} + \tilde{v}\,\tilde{p}) \tag{12}$$

where it is assumed that the canopy has two planes of symmetry, x–z and y–z. Asymmetry about the x–y plane is allowed to account for spanwise camber and the seven constants are defined by Lamb [15]. A canopy of general shape may have has many as 21 constants defining the kinetic energy, however. Typical parafoil canopies will have approximately two planes of symmetry reducing to only seven constants. If spanwise camber is neglected, the canopy can be approximated by an ellipsoid so that H becomes zero. The constants in Eq. (12) can be calculated numerically for a known shape or can be

approximated as discussed in [15–17]. Forces and moments from apparent mass and inertia are found by relating the fluid's momentum to its kinetic energy in a similar way as Lissman and Brown [16], and are summarized in Eqs. (13–17). In the apparent mass contributions, it is assumed that the incidence angle is slowly varying so that its derivative is negligible compared with the body angular rates.

$$\boldsymbol{F}_{\mathrm{AM}} = -[T_{\mathrm{BC}}]^T \left([I_{\mathrm{AM}}] \begin{Bmatrix} \dot{\tilde{u}} \\ \dot{\tilde{v}} \\ \dot{\tilde{w}} \end{Bmatrix} + [I_H] \begin{Bmatrix} \dot{\tilde{p}} \\ \dot{\tilde{q}} \\ \dot{\tilde{r}} \end{Bmatrix} + S^C_{\omega} [I_{\mathrm{AM}}] \begin{Bmatrix} \tilde{u} \\ \tilde{v} \\ \tilde{w} \end{Bmatrix} + S^C_{\omega} [I_H] \begin{Bmatrix} \tilde{p} \\ \tilde{q} \\ \tilde{r} \end{Bmatrix} \right) \tag{13}$$

$$\boldsymbol{M}_{\mathrm{AM}} = -[T_{\mathrm{BC}}]^T \left([I_H] \begin{Bmatrix} \dot{\tilde{u}} \\ \dot{\tilde{v}} \\ \dot{\tilde{w}} \end{Bmatrix} + [I_{\mathrm{AI}}] \begin{Bmatrix} \dot{\tilde{p}} \\ \dot{\tilde{q}} \\ \dot{\tilde{r}} \end{Bmatrix} + S^C_{\omega} [I_H] \begin{Bmatrix} \tilde{u} \\ \tilde{v} \\ \tilde{w} \end{Bmatrix} + S^C_{\omega} [I_{\mathrm{AI}}] + S^C_{V_A} [I_H] \begin{Bmatrix} \tilde{p} \\ \tilde{q} \\ \tilde{r} \end{Bmatrix} \right) \tag{14}$$

$$[I_{\mathrm{AM}}] = \begin{bmatrix} A & 0 & 0 \\ 0 & B & 0 \\ 0 & 0 & C \end{bmatrix} \tag{15}$$

$$[I_{\mathrm{AI}}] = \begin{bmatrix} P & 0 & 0 \\ 0 & Q & 0 \\ 0 & 0 & R \end{bmatrix} \tag{16}$$

$$[I_H] = \begin{bmatrix} 0 & H & 0 \\ H & 0 & 0 \\ 0 & 0 & 0 \end{bmatrix} \tag{17}$$

Notice the forces and moments from apparent mass are a function of the canopy incidence angle. Equations (13) and (14) couple the linear and rotational dynamic in Eqs. (4) and (5). Final dynamic equations of motion are found by substituting all forces and moments into Eqs. (4) and (5), resulting in the matrix solution shown in Eqs. (18) and (20). The common convention is used for tensors of second rank such that $[I'_X] = [T_{\mathrm{BC}}]^T [I_X][T_{\mathrm{BC}}]$ for the quantities in Eqs. (15–17).

$$\Phi = \boldsymbol{F}_A + \boldsymbol{F}_s + \boldsymbol{F}_W - m S^B_{\omega} \begin{Bmatrix} u \\ v \\ w \end{Bmatrix} - [T_{\mathrm{BC}}]^T S^C_{\omega} \left([I_{\mathrm{AM}}] \begin{Bmatrix} \tilde{u} \\ \tilde{v} \\ \tilde{w} \end{Bmatrix} + [I_H] \begin{Bmatrix} \tilde{p} \\ \tilde{q} \\ \tilde{r} \end{Bmatrix} \right) - [I'_{\mathrm{AM}}] S^B_{\omega} [T_{\mathrm{IB}}] \boldsymbol{V}_{A/I} \tag{19}$$

$$\begin{aligned} \mathrm{M} = {} & \boldsymbol{M}_A + S^B_{\mathrm{CG},P} \boldsymbol{F}_A + S^B_{\mathrm{CG},S} \boldsymbol{F}_S - S^B_{\omega} [I_T] \begin{Bmatrix} p \\ q \\ r \end{Bmatrix} \\ & - S^B_{\mathrm{CG},M} [T_{\mathrm{BC}}]^T S^C_{\omega} \left([I_{\mathrm{AM}}] \begin{Bmatrix} \tilde{u} \\ \tilde{v} \\ \tilde{w} \end{Bmatrix} + [I_H] \begin{Bmatrix} \tilde{p} \\ \tilde{q} \\ \tilde{r} \end{Bmatrix} \right) \\ & - [T_{\mathrm{BC}}]^T S^C_{\omega} [I_H] \begin{Bmatrix} \tilde{u} \\ \tilde{v} \\ \tilde{w} \end{Bmatrix} + [T_{\mathrm{BC}}]^T \left(S^C_{\omega} [I_{\mathrm{AI}}] + S^C_{V_{A/I}} [I_H] \right) \begin{Bmatrix} \tilde{p} \\ \tilde{q} \\ \tilde{r} \end{Bmatrix} \\ & - \left(S^B_{\mathrm{CG},M} [I'_{\mathrm{AM}}] + [I'_H] \right) S^B_{\omega} [T_{\mathrm{IB}}] \boldsymbol{V}_{A/I} \end{aligned} \tag{20}$$

The matrix in Eq. (18) appears as an inertia matrix and satisfies many properties of a typical inertia matrix such as symmetry. In the case where all apparent mass and inertia effects are negligible, Eq. (18) reduces to a block diagonal system where linear and rotational dynamic equations decouple. The effective apparent mass and inertia matrices I'_{AM}, I'_H, and I'_{AI} are functions of the canopy incidence angle, so that changing the incidence angle for glide slope control results in varying apparent mass and inertia matrices. This is in contrast to conventional models in which apparent mass and inertia coefficients are assumed constant.

III. Test System

The parafoil system tested is shown in Figs. 2 and 3 with the canopy deployed and undeployed, respectively. The payload of the system consists of a $6 \times 6 \times 18$ in. cardboard box with two avionic boxes on either end. The upper avionics box consists of a data logger with battery, canopy pack, and a Hitec HS-311 servo used to release the packed parafoil. Sensors included in the upper avionics box are three accelerometers, gyroscopes and magnetometers, a global positioning system, and barometric altimeter. The upper box was designed to allow the top flaps of the cardboard box to flare out at a 45 deg angle to allow the undeployed system to be cone stabilized (see Fig. 3). The lower avionics box contains three Hitec HS-785 HB

$$\begin{bmatrix} m\mathrm{I} + [I'_{\mathrm{AM}}] & [I'_H] - [I'_{\mathrm{AM}}] S^B_{\mathrm{CG},M} \\ S^B_{\mathrm{CG},M} [I'_{\mathrm{AM}}] + [I'_H] & I_T + [I'_{\mathrm{AI}}] - [I'_H] S^B_{\mathrm{CG},M} + S^B_{\mathrm{CG},M} ([I'_H] - [I'_{\mathrm{AM}}]) S^B_{\mathrm{CG},M} \end{bmatrix} \begin{Bmatrix} \dot{u} \\ \dot{v} \\ \dot{w} \\ \cdots \\ \dot{p} \\ \dot{q} \\ \dot{r} \end{Bmatrix} = \begin{Bmatrix} \Phi \\ \cdots \\ \mathrm{M} \end{Bmatrix} \tag{18}$$

Fig. 2 Test system with deployed parafoil.

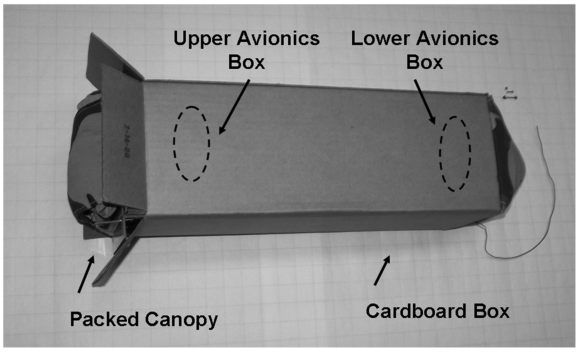

Fig. 3 Test system with undeployed parafoil.

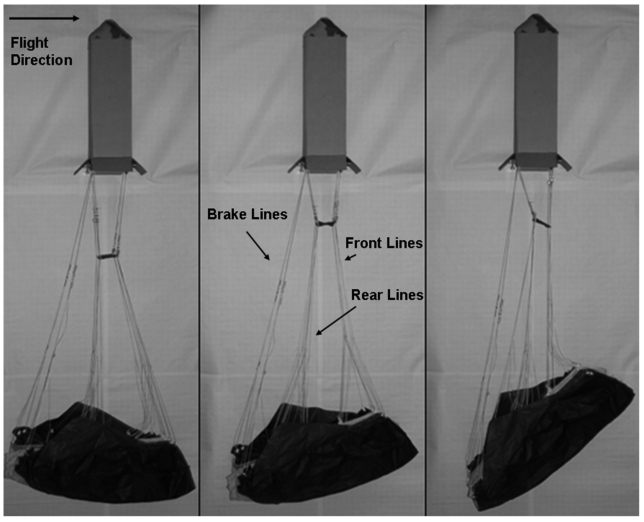

Fig. 4 Parafoil incidence angle change.

sail winches, a Hitec electron 6 FM receiver, and a battery pack. Sail winch 1 and 2 control the right and left brake lines, whereas sail winch three controls the front lines of the parafoil. The sail winch signals are mixed together so that as the front lines are pulled in, the brake lines are let out and vise versa. This allows the geometry of the canopy to accommodate for different incidence angles. Note the rear lines of the canopy remain fixed to the upper box, whereas the brake lines and front lines run through the upper avionics box to the sail winches in the lower avionics box.

As mentioned before, the incidence angle of the parafoil is changed using the three sail winches in the lower avionics box. An example of this incidence change is shown in Fig. 4. Two different parafoil systems were used in this study. Systems 1 and 2 differ mainly in their canopy thickness, leading-edge geometry, and payload weight. The dimensions of the systems are shown in Fig. 5 and outlined in Table 1.

IV. Flight Results

Four flight tests were conducted in low-wind conditions, two for each system. System 1 was configured with a nominal incidence Γ_1 of -6 deg and, once equilibrium was achieved, the incidence angle was changed. In the first flight of system 1, the canopy was rotated down to an incidence Γ_2 of -24 deg, whereas, during the second flight, the canopy was rotated up to an incidence Γ_3 of 10 deg. System 2 was configured with a nominal incidence Γ_4 of -24 deg and was subsequently rotated down to an incidence Γ_5 of -44 deg for both the third and fourth flight tests. Results are shown after canopy opening in Figs. 6–8. Figure 6 shows results for the flight path in which both altitude and distance have been nondimensionalized with respect to the initial altitude. The flight path angle λ can be seen by the slope of the flight path in Fig. 6 and the glide slope (GS) is defined as $-1/\tan(\lambda)$. Table 2 summarizes the four flight tests.

System 1 responds to a decrease in incidence from -6 to -24 deg with a 70% increase in GS, from 1.45 to 2.46. Increasing the incidence from -6 to 10 deg results in a stalled condition where the GS is decreased 89%. System 2 responds in an opposite manner with a decrease in incidence from -24 to -44 deg, resulting in a 48% decrease in GS from 3.70 to 1.94. Differences are also observed in the vertical and forward velocity trends where, for system 1, changing the incidence results in large forward speed changes with vertical speed remaining nearly unchanged, whereas, for system 2, the opposite is true. Results from system 1 were used to estimate C_L and C_D curves for the combined system including payload. The C_L and C_D curves are approximated by a cubic and quadratic curves defined by C_{L0}, $C_{L\alpha}$, $C_{L\alpha 3}$, C_{D0}, and $C_{D\alpha 2}$. Using results for system 1 in Table 2, the coefficients are estimated as 0.28, 0.68, -0.35, 0.135, and 0.95, respectively. Figure 9 shows the estimated curves compared with the measured results for system 1 including canopy and payload. The estimated values are consistent with results from Ware and Hassell [2] who observed maximum lift-to-drag ratios near 2.5, high profile drag and low maximum lift coefficients when compared with a standard rigid wing. It is important to note that, as demonstrated by results from Ware and Hassell [2], the C_L curve is typically flat near stall with the exact angle of attack at stall difficult to define. The C_L curve is approximated well by a cubic function pre- and poststall, however, a higher order function is required to approximate the stall region. The estimated C_L curve in Fig. 9 is valid at angles of attack lower than 30 deg and higher than 70, the location of the maximum C_L can only be identified as occurring within that. Estimation of the stall region is unnecessary because all glide slope control and simulations occur before this region. Simulations of the estimated system GS are shown in Fig. 10 and are consistent with test data.

Table 1 System characteristics

Parameter	System 1	System 2
θ_1, deg	80	50
θ_2, deg	45	45
h, ft	0.35	0.17
b, ft	4.5	5.0
c, ft	2.1	1.3
Weight, lbf	5.23	1.59

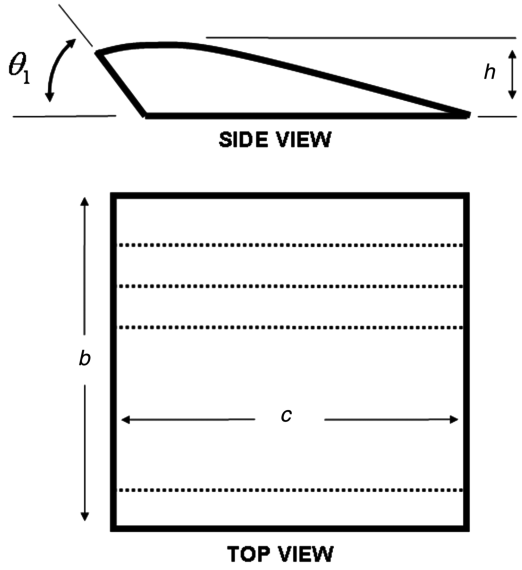

Fig. 5 Canopy geometry.

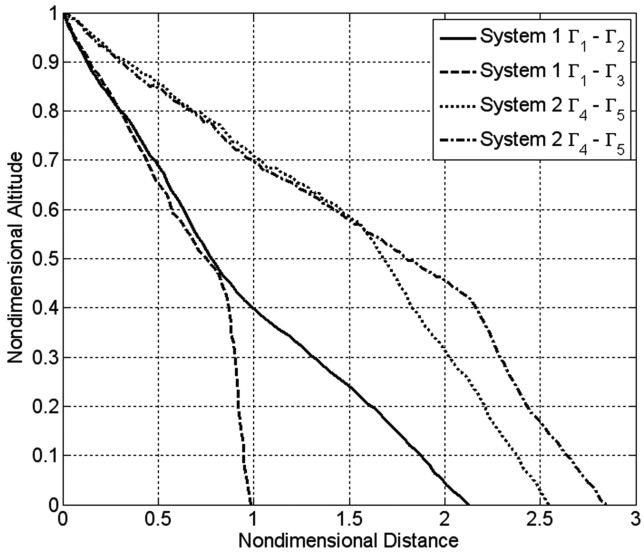

Fig. 6 Flight path angle.

From Fig. 9, system 1 operates to the right of its maximum lift-to-drag ratio for all incidence angles, resulting in an increased GS as the incidence is decreased. Decreasing the incidence of system 2 resulted in a decreased GS, demonstrating system 2 operates to the left of its

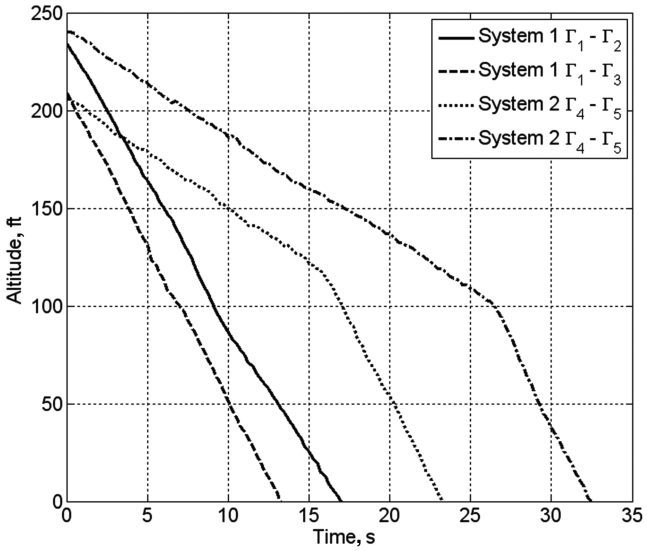

Fig. 7 Altitude.

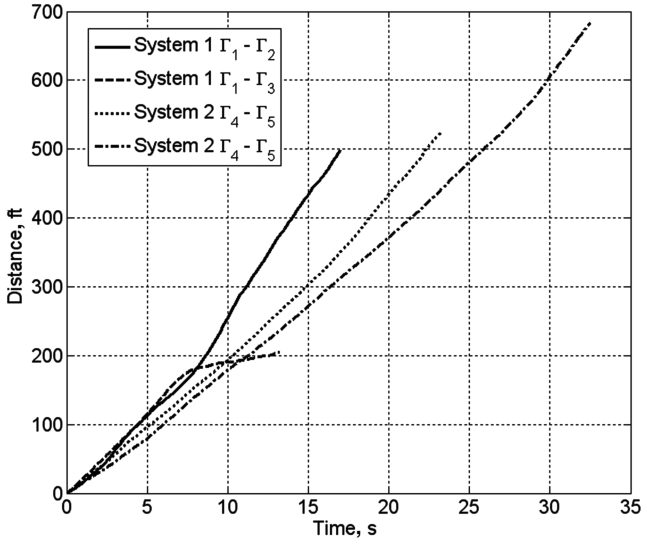

Fig. 8 Distance traveled.

maximum lift-to-drag ratio. Noting that the maximum L/D occurs well before stall, its angle of attack can be estimated using Eq. (21).

$$\alpha_{L/D\max} = \sqrt{\left(\frac{C_{L0}}{C_{L\alpha}}\right)^2 + \frac{C_{D0}}{C_{D\alpha 2}}} - \frac{C_{L0}}{C_{L\alpha}} \tag{21}$$

Equation (21) shows the maximum L/D angle of attack increases as $C_{L\alpha}$ increases and $C_{D\alpha 2}$ decreases, both occurring as the lifting surface efficiency factor increases. This is consistent with system 2 having a small thickness-to-chord ratio, larger aspect ratio, and more rounded nose. Parafoils of higher efficiency will be able to operate to the left of their maximum L/D, whereas an inefficient canopy may operate to the right. It is demonstrated by systems 1 and 2 that a parafoil system can effectively operate on either side of the

Table 2 Flight-test summary

	System 1 $\Gamma_1 = -6$ deg	System 1 $\Gamma_2 = -24$ deg	System 1 $\Gamma_3 = 10$ deg	System 2 $\Gamma_4 = -24$ deg	System 2 $\Gamma_5 = -44$ deg
α, deg	28	6	70	10	5
Glide slope	1.45	2.46	0.28	3.70	1.94
Speed, ft/s	26	35	16	21	26
C_L	0.56	0.35	0.49	0.45	0.27

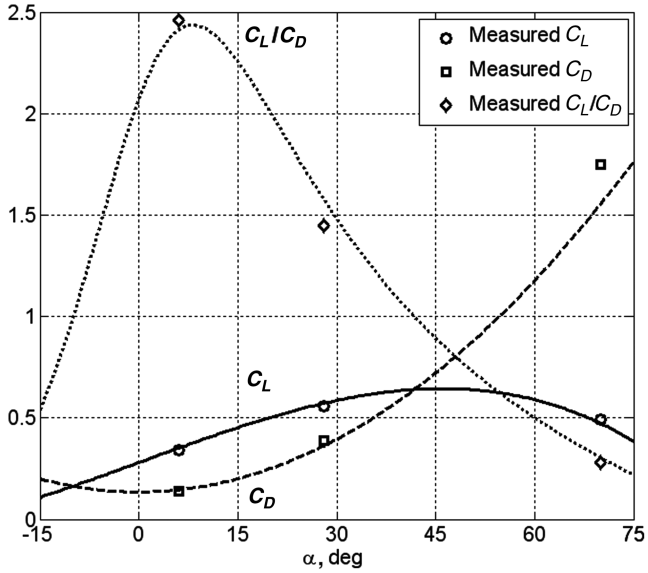

Fig. 9 Estimated lift coefficient, drag coefficient, and C_L/C_D for system 1 including payload.

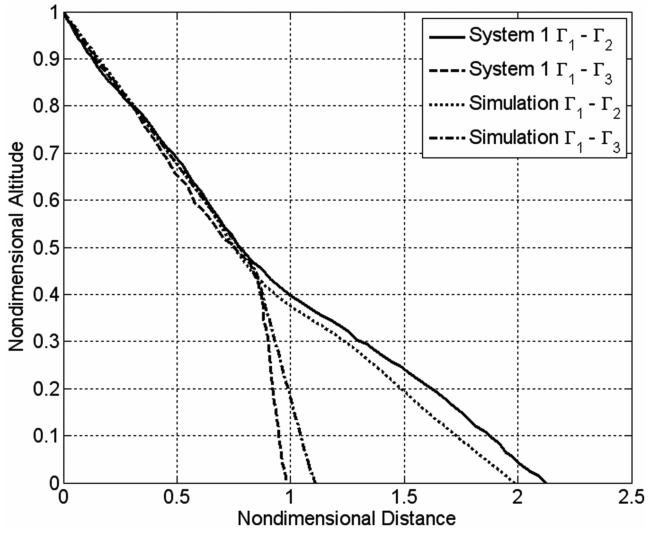

Fig. 10 Comparison of simulated and measured GS for system 1.

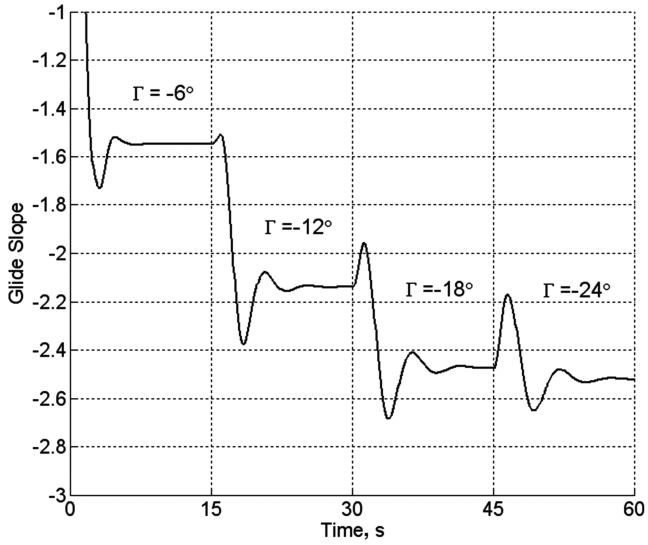

Fig. 11 Simulated GS varying incidence Γ of system 1.

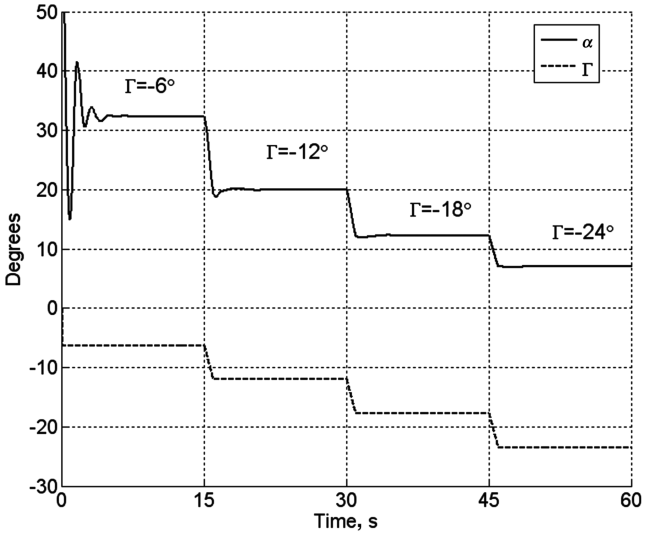

Fig. 12 Simulated angle of attack varying incidence Γ of system 1.

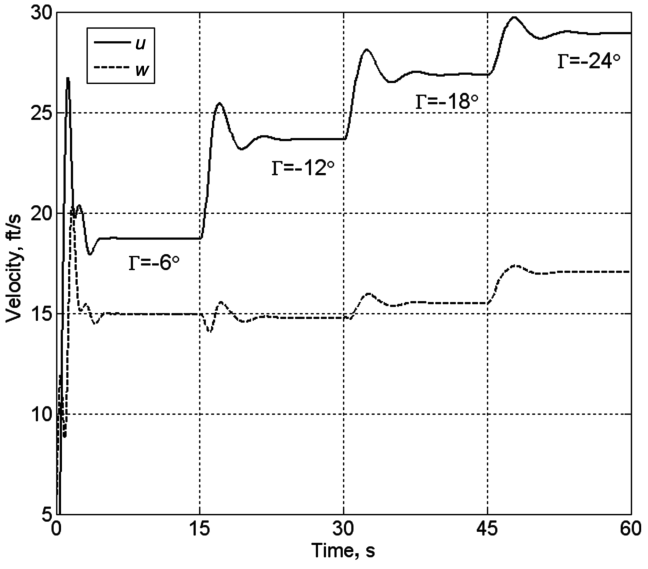

Fig. 13 Simulated velocities varying incidence Γ of system 1.

maximum L/D angle of attack and have effective glide slope control. A system, however, may be arranged such that it operates near its maximum L/D, in such a case, minimal glide slope control will result from the small slope of the L/D curve in this vicinity.

Simulations were completed for system 1 in which the incidence was decreased from -6 to -12, -18, and -24 deg at 15 s intervals with each change occurring linearly over a second. Figure 11 shows the glide slope dynamics persist for 5 s after each change in incidence. The GS initially decreases in response to the decreased lift from decreasing angle of attack before it increases as the speed increases. Changes in angle of attack and velocities are shown in Figs. 12 and 13, respectively. As incidence is decreased, the angle of attack decreases approaching the maximum L/D where GS control authority diminishes. A nearly linear GS mechanism can be implemented for system 1 by designing the nominal incidence to be -12 deg, so that $\pm 25\%$ changes in GS can be achieved over a -6–-18 incidence range. If maximum L/D flight is desired, system 1 can be flown at an incidence of -18 deg, however, the GS can only be effectively decreased.

V. Precision Placement Algorithm

The precision placement trajectory tracking algorithm used here is based on a model predictive control (MPC) scheme that tracks

desired heading and was successfully demonstrated on a small parafoil by Slegers and Costello [18]. It was also shown in [18] that linearization of a parafoil model results in the lateral dynamics being decoupled from longitudinal dynamics. Consider a single input/single output (SISO) linear discrete system described in state-space form as given in Eq. (22).

$$x_{k+1} = \mathbf{A}x_k + \mathbf{B}u_k \qquad y_k = \mathbf{C}x_k \tag{22}$$

Assume the system matrices $\mathbf{A}$, $\mathbf{B}$, and $\mathbf{C}$ are known and that x_k is the state vector $[\phi_k \quad \psi_k \quad p_k \quad r_k]^T$, u_k is the asymmetric brake deflection δ_a, and y_k is the output ψ_k at time k. The preceding model can be used to estimate the future state of the system. Assuming a desired trajectory is known, an estimated error signal $\tilde{e}_k = \bar{y}_k - \tilde{y}_k$ is computed over a finite set of future time instants called the prediction horizon H_p, where $\bar{y}_k$ and $\tilde{y}_k$ represent the desired output and an estimated quantity at time k. In model predictive control, the control computation problem is cast as a finite time discrete optimal control problem. To compute the control input at a given time instant, a quadratic cost function is minimized through the selection of the control history over the control horizon. The cost function can be written as

$$J = (\bar{Y} - \tilde{Y})^T(\bar{Y} - \tilde{Y}) + U^T R U \tag{23}$$

where

$$\bar{Y} = \{\, \bar{Y}_{k+1} \quad \bar{Y}_{k+2} \quad \ldots \quad \bar{Y}_{k+H_p} \,\}^T \tag{24}$$

$$\tilde{Y} = K_{\mathrm{CA}}x_k + K_{\mathrm{CAB}}U \tag{25}$$

$$U = \{\, u_k \quad u_k \quad \ldots \quad u_{k+H_p-1} \,\}^T \tag{26}$$

and R is a symmetric positive semidefinite weighting matrix penalizing control having size H_p. Equation (25) is used to express the predicted output vector $\tilde{Y}$ in terms of the system matrices.

$$K_{\mathrm{CA}} = \begin{bmatrix} \mathbf{CA} \\ \mathbf{CA}^2 \\ \vdots \\ \mathbf{CA}^{H_p} \end{bmatrix} \tag{27}$$

$$K_{\mathrm{CAB}} = \begin{bmatrix} \mathbf{CB} & \mathbf{0} & \mathbf{0} & \mathbf{0} & \mathbf{0} \\ \mathbf{CAB} & \mathbf{CB} & \mathbf{0} & \mathbf{0} & \mathbf{0} \\ \mathbf{CA}^2\mathbf{B} & \mathbf{CAB} & \mathbf{CB} & \mathbf{0} & \mathbf{0} \\ \vdots & \vdots & & \ddots & \mathbf{0} \\ \mathbf{CA}^{H_p-1}\mathbf{B} & \cdots & \mathbf{CA}^2\mathbf{B} & \mathbf{CAB} & \mathbf{CB} \end{bmatrix} \tag{28}$$

Equations (25) and (26) can be substituted into the cost function of Eq. (23) resulting in Eq. (29), that is in terms of the system state x_k, desired trajectory $\bar{Y}$, control vector $\boldsymbol{U}$, and system matrices $\mathbf{A}$, $\mathbf{B}$, $\mathbf{C}$, and R.

$$J = (\bar{Y} - K_{\mathrm{CA}}x_k - K_{\mathrm{CAB}}\boldsymbol{U})^T(\bar{Y} - K_{\mathrm{CA}}x_k - K_{\mathrm{CAB}}\boldsymbol{U}) + \boldsymbol{U}^T R \boldsymbol{U} \tag{29}$$

The control $\boldsymbol{U}$, which minimizes Eq. (29), is

$$\boldsymbol{U} = K(\bar{Y} - K_{\mathrm{CA}}x_k) \tag{30}$$

where

$$\mathrm{K} = (K_{\mathrm{CAB}}^T K_{\mathrm{CAB}} + R)^{-1} K_{\mathrm{CAB}}^T \tag{31}$$

Equation (30) contains the optimal control input over the entire control horizon, however, at time k only the first element u_k is needed. The first element u_k can be extracted from Eq. (30) by defining K_1 as the first row of K. The final expression for an optimal control at the next time sample is given in Eq. (18), where a description of estimating the desired heading for a parafoil is provided in [18].

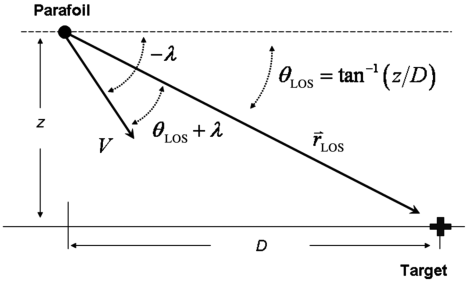

Fig. 14 Glide slope guidance geometry.

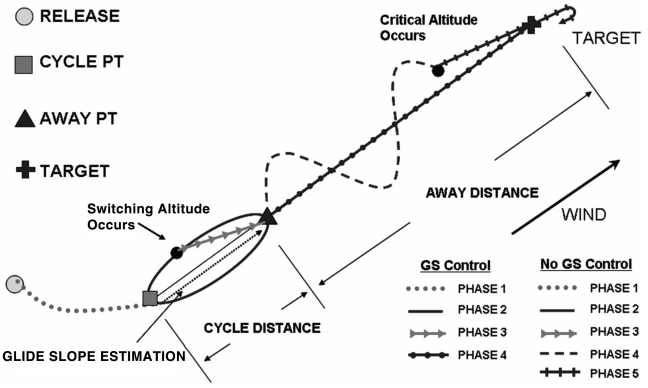

Fig. 15 Phases of precision placement algorithm.

$$u_k = \mathrm{K}_1(\bar{Y} - K_{\mathrm{CA}}x_k) \tag{32}$$

Glide slope control is treated separately from heading tracking and is implemented similar to proportional navigation of guided missiles. A diagram of the glide slope guidance is shown in Fig. 14 where r_{LOS} is the line-of-sight vector from the parafoil to the target. As the parafoil approaches the target, any misalignment of the velocity vector and r_{LOS} will result in r_{LOS} rotating with the angular velocity ω_{LOS} provided in Eq. (33). For the parafoil to impact the target, the angular velocity of the line-of-sight vector ω_{LOS} must be zero; if the parafoil is falling too fast or too slow, ω_{LOS} will be positive or negative, respectively. A discrete proportional-integral controller, shown in Eq. (34), uses incidence angle to track zero ω_{LOS}, thus placing the system on the required GS to impact the target. In Eq. (34), the angular velocity ω_{LOS} is sampled at intervals of ΔT.

$$\omega_{\mathrm{LOS}} = \frac{V}{D}\sin(\theta_{\mathrm{LOS}} + \lambda) \tag{33}$$

$$\Gamma_k = \Gamma_{k-1} + (K_p + K_i\Delta T/2)\omega_{\mathrm{LOS}}, k - (K_p - K_i\Delta T/2)\omega_{\mathrm{LOS},k-1} \tag{34}$$

The MPC algorithm requires a desired heading trajectory which is defined by four parameters: target location, away distance, cycle distance, and wind heading angle. As shown in Fig. 15, these four parameters define three fixed tracking points: target point, away point, and cycle point. Using these three points, precision placement objectives are divided into four phases when glide slope control is implemented and five phases otherwise. The phases are pictured in Fig. 15 and defined as follows:

Phase 1: The system is released upwind to ensure it reaches the target in strong winds. System travels a direct path to the cycle point.

Phase 2: System circles around the away and cycle point. Downwind glide slope is estimated when traveling toward the target point. This continues until the switch altitude is reached. The switch

Table 3 Parafoil and payload physical parameters

Parameter	Value	Units
I_{XX}	0.312	slug · ft^2
I_{YY}	0.296	slug · ft^2
I_{ZZ}	0.039	slug · ft^2
I_{XZ}	0.022	slug · ft^2
$C_{Y\beta}$	−0.20	——
C_{lp}	−0.15	——
$C_{l\delta a}$	−0.005	——
C_{mq}	−0.40	——
C_{nr}	−0.09	——
$C_{n\delta a}$	0.007	——
C_{DS}	0.30	——
S_S	0.65	ft^2
A	0.0008	slug
B	0.0022	slug
C	0.0290	slug
H	0.0014	slug
P	0.040	slug · ft^2
Q	0.100	slug · ft^2
R	0.0018	slug · ft^2

altitude is defined as the distance to the target divided by the estimated glide slope plus an excess altitude. Excess altitude is only required when glide slope control is absent. Excess altitude allows the system to turn to the target early, because when GS control is absent, the effective GS cannot be increased, only reduced, by swerving.

Phase 3: System travels directly to the away point. Glide slope estimation is terminated.

Phase 4: With no GS control, system continues glide slope estimation. At each update time, the distance to the target and a distance to waste are calculated. MPC turns left and right, tracking an "S" trajectory generated by waypoints to waste an appropriate distance to impact the target. With GS control, at each update time, the angular velocity of the line-of-sight vector ω_{LOS} is calculated and a proportional-integral controller regulates it to zero. MPC tracks a path directly to the target.

Phase 5: The system flies directly to the target once a critical altitude is achieved.

Nominal simulations of the precision placement algorithm with MPC were performed for the canopy and payload of system 1. The nominal incidence is −12 deg and physical parameters are listed in Table 3. Aerodynamic coefficients listed in Table 3 were estimated from dynamic maneuvers during flight testing. The discrete linear matrices used for MPC are provided in Eqs. (35) and (36) where the discretization period is 0.5 s. The system is released from an altitude of 2500 ft, 2500 ft downrange and 150 ft cross range with a desired target at the origin. Away and cycle distance are 2000 and 1000 ft, respectively. Without GS control, the critical and excess altitudes are 100 and 200 ft, respectively. A 5 ft/s tailwind rotated 10 deg with respect to the target line is used both with and without GS control. Results are shown in Figs. 16–20 where both methods impact within 15 ft of the target. Phases 1 and 2 are identical for both methods. Phase 3 is entered sooner without GS control as seen in Figs. 16 and 17 because of the required excess altitude. Phase 3 is entered at an altitude of 1250 ft at 103 s without GS control and 1050 ft at 111 s with GS control. Phase 4 is entered at 132 s without GS control and at 140 s with GS control. During phase 4, the system with GS control varies the canopy incidence and angle of attack to adjust for errors in GS, as seen in Figs. 18 and 19. The system without GS control swerves left and right to adjust the effective GS, requiring more active brake maneuvers in the final stages, as shown in Fig. 20. An advantage of GS control is seen during the fourth phase. Over the last 2000 ft of range, the system with GS control maintains a constant orientation with respect to the target and wind, enabling accurate GS estimation. Swerving required by the system without GS control changes the orientation with respect to the wind. As the system faces toward positive and negative cross range, the wind slows and increases the forward speed, respectively. Changing speeds make

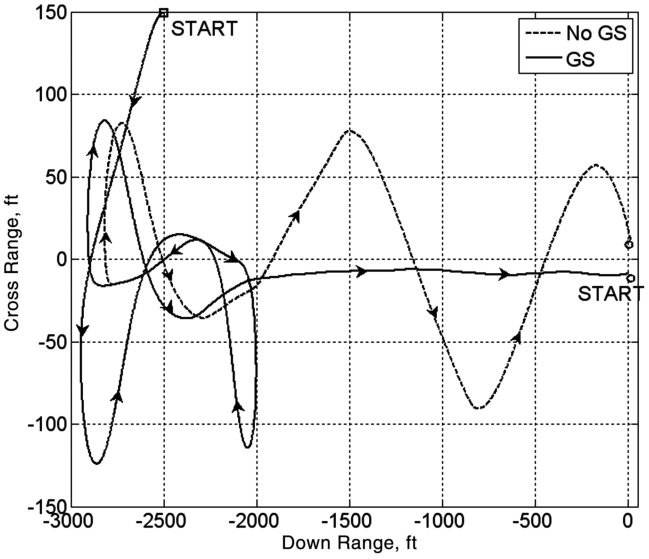

Fig. 16 Simulated precision placement cross range.

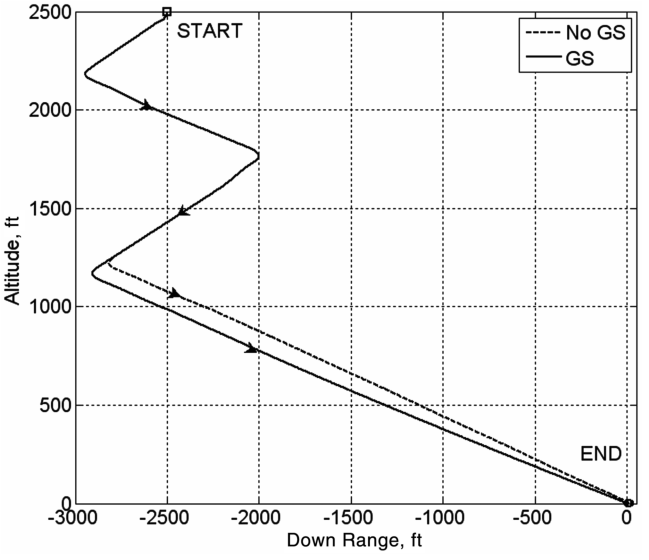

Fig. 17 Simulated precision placement altitude.

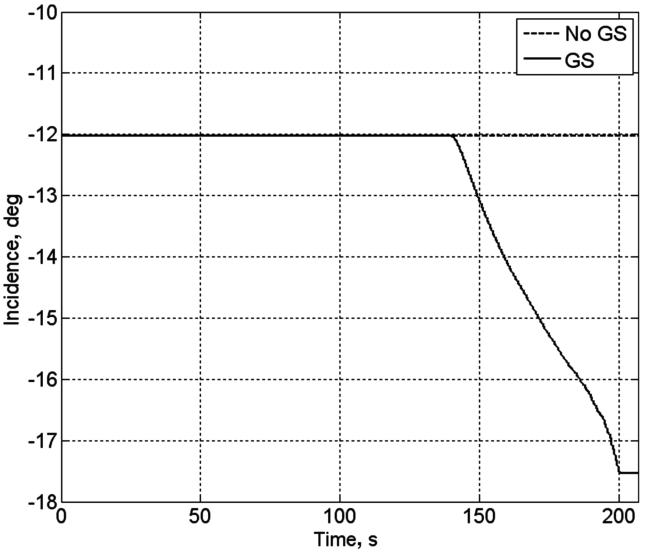

Fig. 18 Simulated precision placement incidence angle.

accurate GS estimation more difficult, while the variation in cross range induces additional errors in impact.

$$\mathbf{A} = \begin{bmatrix} 0.899 & 0 & 0.180 & 0.020 \\ 0.008 & 1.000 & 0.001 & 0.033 \\ -0.119 & 0 & -0.017 & -0.002 \\ 0.008 & 0 & 0.002 & 0.000 \end{bmatrix} \tag{35}$$

$$\mathbf{B} = \begin{bmatrix} 0.001 \\ 0.101 \\ -0.012 \\ 0.104 \end{bmatrix} \tag{36}$$

VI. Precision Placement Results

Monte Carlo simulations of 100 drops were completed using the precision placement algorithm with MPC. Noise was injected into GPS, altitude, and inertial measurement unit (IMU) sensors. In addition to sensor errors, three sources of wind variation were added to the simulation: wind shear, varying magnitude, and direction. The wind was divided into two segments varied independently, namely, wind above 1000 ft and wind below 1000 ft, to simulate inconsistent wind profiles. Prevailing wind was assumed by the system to come from a heading of 0 deg, while true wind varied in its direction. For all simulations, the target was set as the origin. Sensor noise and wind variation statistics are listed in Table 4.

Table 4 Error statistics

Parameter	Mean	Standard deviation
Initial condition position X	3500 ft	750 ft
Initial condition position Y	0 ft	750 ft
Initial condition position Z	4500 ft	750 ft
GPS X bias	0.0 ft	3.0 ft
GPS Y bias	0.0 ft	3.0 ft
GPS X deviation	1.0 ft	0.0 ft
GPS Y deviation	1.0 ft	0.0 ft
Altitude bias	0.0 ft	5.0 ft
Altitude variation	1.0 ft	0.0 ft
Roll, pitch, and yaw bias	0.0 deg	1.7 deg
Roll, pitch, and yaw deviation	1.7 deg	0.0 deg
u, v, and w bias	0.0 ft/s	0.1 ft/s
u, v, and w deviation	0.7 ft/s	0.0 ft/s
p, q, and r bias	0.0 deg	1.7 deg
p, q, and r deviation	1.0 deg	0.0 deg
Wind1	10.0 ft/s	3.0 ft/s
Wind2	10.0 ft/s	3.0 ft/s
Wind heading error	0.0 deg	11.0 deg

Monte Carlo simulations were first completed with and without GS control including sensor errors and no wind. Dispersion results are shown in Fig. 21, whereas histograms are provided in Figs. 22 and 23. The circular error probable (CEP) defined by the radius, which includes 50% of the impacts, are shown by a circle. CEP with and without GS control are 9.8 and 13.2 ft, respectively, with dispersion patterns being similar in both cases. The main difference is found in the histograms in which, without GS control, impacts are skewed toward larger errors, where 5% of impacts have more than 30 ft of error. With GS control, no impact has more than 30 ft of error.

Results including both sensor errors and wind variations are shown in Figs. 24–26. CEP with and without GS control are 16.7 and 72.4 ft, respectively. Including winds, the GS control CEP increased by only 70%, whereas the CEP without GS control increased 450%. Including GS control, a reduction by more than a factor of three is achieved in CEP and sensitivity to winds is reduced. Dispersion patterns also differ significantly. With GS control, the dispersion is

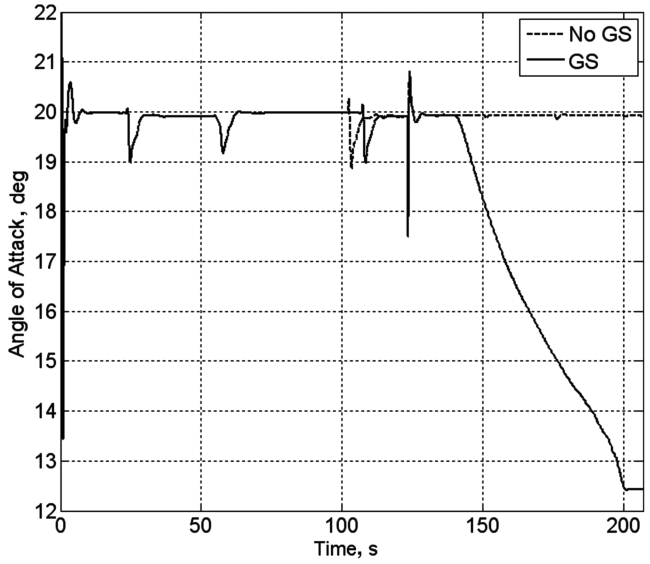

Fig. 19 Simulated precision placement angle of attack.

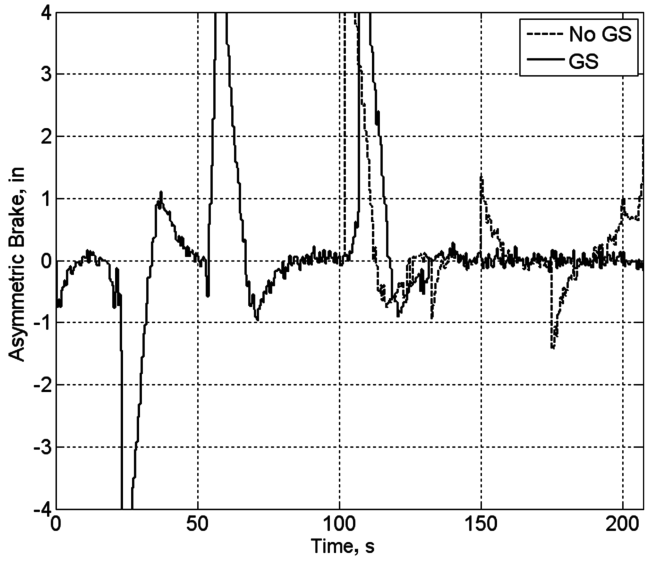

Fig. 20 Simulated precision placement asymmetric control.

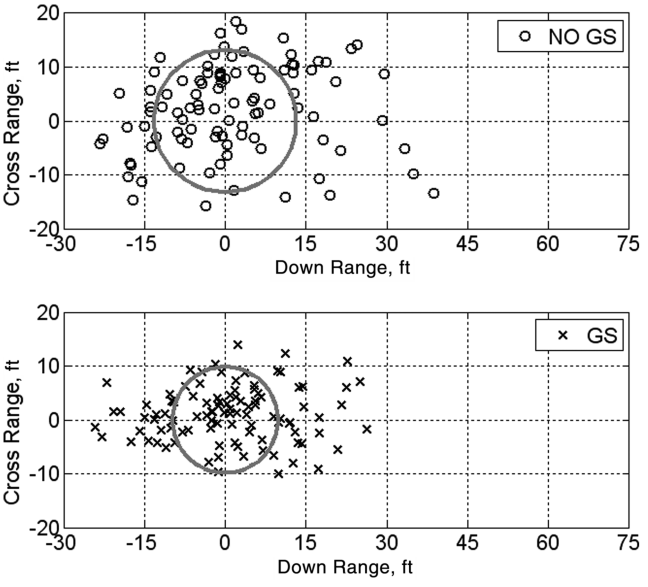

Fig. 21 Dispersion for all sensor errors and no wind.

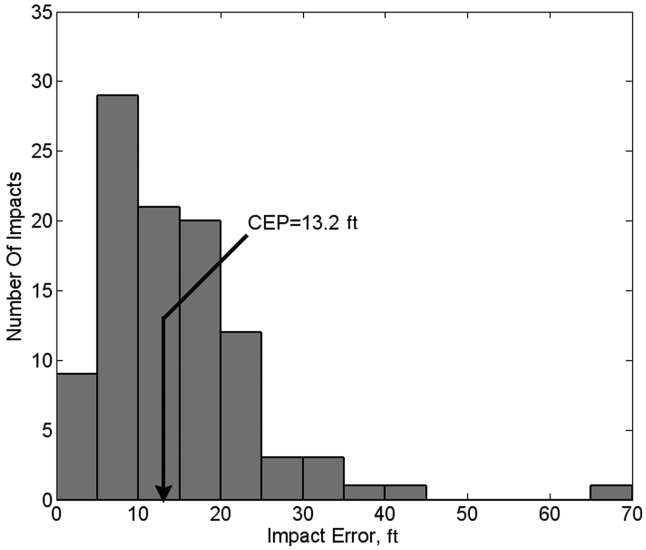

Fig. 22 Without GS control histogram for sensor errors and no wind.

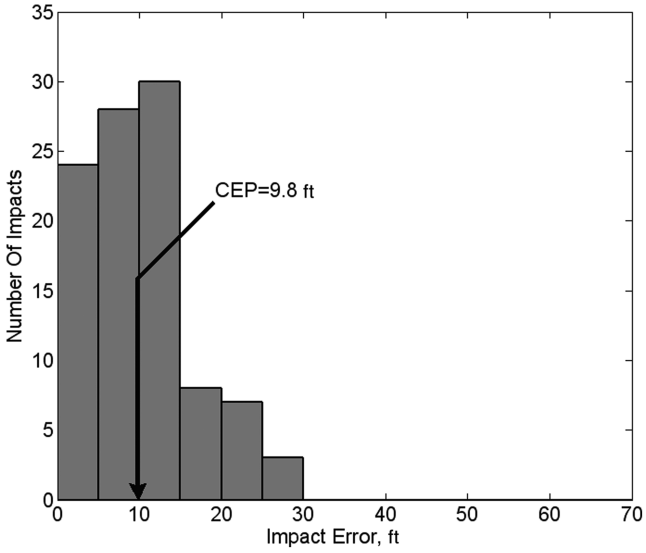

Fig. 23 GS control histogram for sensor errors and no wind.

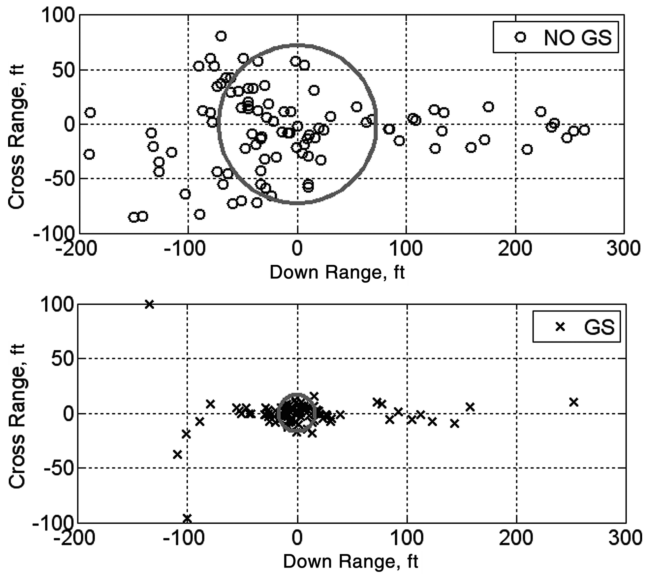

Fig. 24 Dispersion for all sensor errors and varying wind.

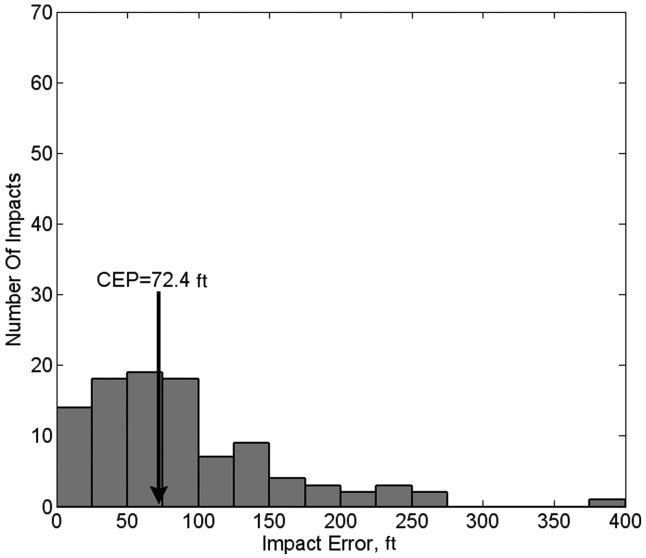

Fig. 25 No GS control histogram for sensor errors and varying winds.

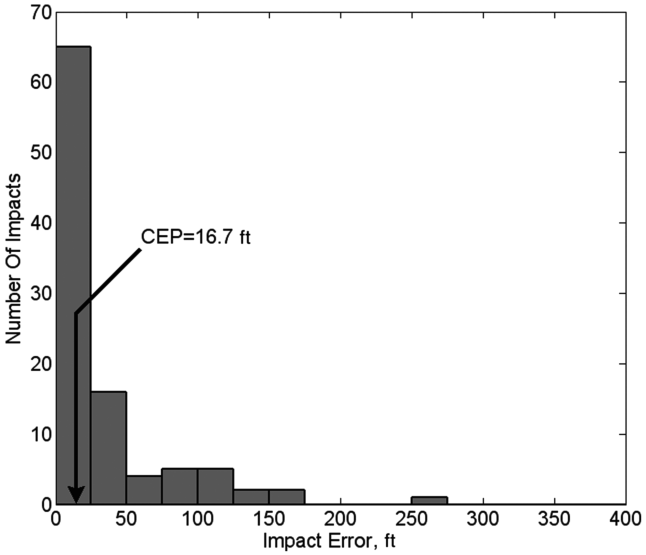

Fig. 26 GS control histogram for sensor errors and varying winds.

mainly in range with 97% of the cases having less than 20 ft of cross-range error. Swerving required without GS control increased dispersion in cross range. GS control also reduced errors greater than 200 ft from 11 to 1.

VII. Conclusions

Glide slope control was demonstrated with two parafoil systems. One system experienced increased glide slope from decreasing the incidence angle whereas the other experienced the opposite. The location of the system's angle of attack on the L/D curve determined the response. Parafoils of higher efficiency possessing smaller thickness-to-chord ratios, larger aspect ratios, and rounded nose may operate to the left of their maximum L/D. Inefficient canopies may tend to operate to the right. Effective GS control can be achieved in either case. GS control becomes minimal when operating near the maximum L/D.

Precision placement was demonstrated with and without GS control. Without GS control, the parafoil swerves left and right to change the effective GS toward the target. With GS control, the incidence angle is controlled to place the system on a desired GS while traveling directly toward the target. Monte Carlo simulations completed with sensor errors and no wind showed successful

precision placement in both cases. Using GS control, the CEP was slightly lower, 9.8 ft compared with 13.2 ft without. In the presence of uncertain winds, GS control reduced the CEP by a factor of three compared with no GS control. The resulting improvement was a result of improved GS estimation by traveling the same direction and a reduction in cross-range error by not requiring swerve maneuvers.

References

[1] Slegers, N., and Costello, M., "Aspects of Control for a Parafoil and Payload System," *Journal of Guidance, Control, and Dynamics*, Vol. 26, No. 6, 2003, pp. 898–905.

[2] Ware, G., and Hassell, J., "Wind-Tunnel Investigation of Ram-Air_Inflated All-Flexible Wings of Aspect Ratios 1.0 to 3.0," NASA TM SX-1923, 1969.

[3] Brown, G., "Parafoil Steady Turn Response to Control Input," AIAA Paper 93-1241, May 1993.

[4] Hailiang, M., and Zizeng, Q., "9-DOF Simulation of Controllable Parafoil System for Gliding and Stability," *Journal of National University of Defense Technology*, Vol. 16, No. 2, 1994, pp. 49–54.

[5] DeTurris, D., Ervin, J., and Alptekin, S., "Development of an Autonomous Tactical Reconnaissance Platform," AIAA Paper 2003-2117, May 2003.

[6] Altmann, H., and Windl, J., "ParaLander: A Medium-Weight Demonstrator for Autonomous, Range-Optimized Aerial Cargo Delivery," AIAA Paper 2005-1627, May 2005.

[7] Jann, T., "Advanced Features for Autonomous Parafoil Guidance, Navigation and Control," AIAA Paper 2005-1642, May 2005.

[8] Bennett, T., and Fox, R., "Design, Development & Flight Testing of the NASA X-38 7500 ft2 Parafoil Recovery System," AIAA Paper 2003-2107, May 2003.

[9] Madsen, C., Sostaric, R., and Cerimele, C., "Flight Performance, Aerodynamics, and Simulation Development for the X-38 Parafoil Test Program," AIAA Paper 2003-2108, May 2003.

[10] George, S., Carter, D., Berland, J., Dunker, S., Tavan, S., and Barber, J., "Dragonfly 4,500 kg Class Guided Airdrop System," AIAA Paper 2005-7095, Sept. 2005.

[11] Zhu, Y., Moreau, M., Accorsi, M., Leonard, J., and Smith, J., "Computer Simulation of Parafoil Dynamics," AIAA Paper 2001-2005, May 2001.

[12] Gupta, M., Xu, Z., Zhang, W., Accorsi, M., Leonard, J., Benney, R., and Stein, K., "Recent Advances in Structural Modeling of Parachute Dynamics," AIAA Paper 2001-2030, May 2001.

[13] Iacomini, C., and Cerimele, C., "Lateral-Directional Aerodynamics from a Large Scale Parafoil Test Program," AIAA Paper 99-1731, June 1999.

[14] Iacomini, C., and Cerimele, C., "Longitudinal Aerodynamics from a Large Scale Parafoil Test Program," AIAA Paper 99-1732, June 1999.

[15] Lamb, H., *Hydrodynamics*, Dover, New York, 1945, pp. 160–174.

[16] Lissaman, P., and Brown, G., "Apparent Mass Effects on Parafoil Dynamics," AIAA Paper 93-1236, May 1993.

[17] Barrows, T., "Apparent Mass of Parafoils with Spanwise Camber," *Journal of Aircraft*, Vol. 39, No. 3, 2002, pp. 445–451.

[18] Slegers, N., and Costello, M., "Model Predictive Control of a Parafoil and Payload System," *Journal of Guidance, Control, and Dynamics*, Vol. 28, No. 4, 2005, pp. 816–821.